EDGE ARTICLE

Solvent-mediated precipitating synthesis and optical properties of polyhydrido Cu_{13} nanoclusters with four vertex-sharing tetrahedrons†

Xinzhang Lin, [ad] Jie Tang,[ad] Chenyu Zhu,[a] Li Wang,[b] Yang Yang,[ad] Ren'an Wu, [b] Hongjun Fan [*c] Chao Liu [*a] and Jiahui Huang [*a]

Structurally defined metal nanoclusters facilitate mechanism studies and promote functional applications. However, precisely constructing copper nanoclusters remains a long-standing challenge in nanoscience. Developing new efficient synthetic strategies for Cu nanoclusters is highly desirable. Here, we propose a solvent-mediated precipitating synthesis (SMPS) to prepare $Cu_{13}H_{10}(SR)_3(PPh_3)_7$ nanoclusters (H–SR = 2-chloro-4-fluorobenzenethiol). The obtained Cu_{13} nanoclusters are high purity and high yield (39.5%, based on Cu atom), proving the superiority of the SMPS method. The Cu_{13} nanoclusters were comprehensively studied *via* a series of characterizations. Single crystal X-ray crystallography shows that the Cu_{13} nanoclusters contain a threefold symmetry axis and the Cu_{13} kernel is protected by a monolayer of ligands, including PPh_3 and thiolates. Unprecedentedly, the aesthetic Cu_{13} kernel is composed of four vertex-sharing tetrahedrons, rather than the common icosahedral or cuboctahedral M_{13}. The intramolecular $\pi \cdots \pi$ interactions between thiolates and PPh_3 on the surface contribute to the stable configuration. Furthermore, electrospray ionization mass spectrometry (ESI-MS) and nuclear magnetic resonance (NMR) revealed the existence of ten hydrides, including four types of hydrides. Density functional theory (DFT) calculations without simplifying the ligands simulated the location of the 10 hydrides in the crystal structure. Additionally, the steady-state ultraviolet-visible absorption and fluorescence spectra of the Cu_{13} nanoclusters exhibit unique optical absorbance and photoluminescence. The ultrafast relaxation dynamics were also studied *via* transient absorption spectroscopy, and the three decay components are attributed to the relaxation pathways of internal conversion, structural relaxation and radiative relaxation. This work provides not only a novel SMPS strategy to efficiently synthesize Cu_{13} nanoclusters, but also a better insight into the structural characteristics and optical properties of the Cu nanoclusters.

Introduction

Copper has exerted a profound influence on human society since the Bronze Age. Atomically precise copper nanoclusters protected by organic ligands have been on the upsurge in nanoscience during the last decade.[1–5] Copper-based nanomaterials play a crucial role in the applications of energy conversion,[6,7] bio-imaging[8] and chemical sensing,[9] *etc.* For example, copper is the dominant metal catalyst for the production of hydrocarbons through the electrochemical reduction of CO_2.[10,11] Additionally, metal nanoclusters exhibit a discrete electronic structure originating from quantum size effects and provide a novel opportunity for engineering their abundant molecular-like properties.[12–14] The well-defined atomic composition and precise crystal structure of nano-clusters are beneficial for exploring their formation mechanism and catalytic mechanism and constructing structure–property relationships at the atomic level.[15,16] Therefore, the controllable synthesis and structure determination of copper nanoclusters are of critical importance in nanotechnology. Over the decades, tremendous progress has been achieved in organic-ligand-protected Au and Ag nanoclusters, such as Au_{25},[17–19] Au_{40},[20–22] Au_{60},[23,24] Au_{92},[25,26] Au_{110},[27] Au_{279},[28] Ag_{25},[29] Ag_{78},[14,30] Ag_{141},[31] Ag_{374},[32] *etc.* In contrast, the number of Cu nanoclusters is extremely limited owing to the high susceptibility towards

a Dalian National Laboratory for Clean Energy, Dalian Institute of Chemical Physics, Chinese Academy of Sciences, Dalian 116023, China. E-mail: chaoliu@dicp.ac.cn; jiahuihuang@dicp.ac.cn

b Laboratory of High-Resolution Mass Spectrometry Technologies, Dalian Institute of Chemical Physics, Chinese Academy of Sciences, Dalian 116023, China

c State Key Laboratory of Molecular Reaction Dynamics, Dalian Institute of Chemical Physics, Chinese Academy of Sciences, Dalian 116023, China. E-mail: fanhj@dicp.ac.cn

d University of Chinese Academy of Sciences, Beijing 100049, China

† Electronic supplementary information (ESI) available: Detailed crystallographic structure analysis, NMR and molecular orbits for $Cu_{13}H_{10}(SR)_3(PPh_3)_7$ nanoclusters. CCDC 2170868. For ESI and crystallographic data in CIF or other electronic format see DOI: https://doi.org/10.1039/d2sc06099j

oxidation of Cu. A handful of ligand-protected Cu nanoclusters have been synthesized and structurally characterized, such as Cu_{11},[33,34] Cu_{13},[35–38] Cu_{15},[4] Cu_{18},[39,40] Cu_{20},[41–43] Cu_{23},[5,44,45] Cu_{25},[40,46,47] Cu_{28},[48] Cu_{32},[49,50] Cu_{36},[1] Cu_{53},[51,52] Cu_{61},[53] Cu_{81},[54] etc. Nevertheless, compared with Au and Ag nanoclusters, the library of Cu nanoclusters requires further enrichment and expansion. However, the efficient synthesis of Cu nanoclusters still remains challenging.

The synthetic methods for Cu nanoclusters have generally followed those of Au and Ag nanoclusters. The Brust–Schiffrin method,[55] a general strategy for Au nanoclusters, is also appropriate to synthesize Cu nanoclusters. Chen et al. prepared mixed-size Cu_n ($n \leq 8$) nanoclusters using this method.[56] Moreover, Sun et al. utilized the gradient reduction strategy with Cu powder and Ph_2SiH_2 as reductants, respectively, to obtain Cu_{23} nanoclusters.[5] Zheng et al. designed a diamine-assisted synthetic strategy to construct Cu_{32} nanoclusters in an inert atmosphere.[50] Bakr et al. presented a one-pot direct reduction strategy to synthesize Cu_{81} nanoclusters.[54] Additionally, some other synthetic approaches for Cu nanoclusters have also been reported, including a water-in-oil microemulsion strategy, electrochemical synthesis, microwave-assisted polyol synthesis, etc.[57,58] Although researchers have tried their best to develop the synthesis of Cu nanoclusters, effective synthetic strategies to obtain more Cu nanoclusters are still lacking. In addition, difficult separation, low yields and complicated procedures are limitations in the synthetic process. Therefore, designing and developing novel synthetic strategies to efficiently boost the purity and yield of Cu nanoclusters is of great importance and significance.

Herein, we develop a solvent-mediated precipitating synthesis (SMPS) to prepare a polyhydrido Cu nanocluster formulated as $Cu_{13}H_{10}(SR)_3(PPh_3)_7$ (Cu_{13} for short). The SMPS is an efficient strategy to synthesize high-purity Cu_{13} nanoclusters in high yield. X-ray crystallographic analysis revealed that Cu_{13} nanoclusters have a threefold symmetry axis and comprise a Cu_{13} kernel with three types of exterior ligands. The Cu_{13} kernel consists of four vertex-sharing tetrahedrons, making it quite different from the common icosahedral or cuboctahedral M_{13} kernels. The intramolecular $\pi\cdots\pi$ interactions between thiolates and PPh_3 are favorable to the configurational stability. ESI-MS and NMR analysis confirmed the molecular composition of the Cu_{13} nanoclusters including the number and type of hydrides. DFT was carried out to simulate the UV-vis absorption, electronic structure and location of the 10 hydrides for the nanocluster. Of note, to obtain accurate results, DFT calculations were performed using the entire structure of the Cu_{13} nanoclusters, without the conventional substitution of $H–SCH_3$ for $H–SR$. Furthermore, the UV-vis absorption spectrum of the Cu_{13} nanoclusters exhibits multiple broad absorption peaks, while the emission spectrum exhibits three obvious peaks at 408, 434 and 458 nm, respectively. The transient absorption spectra revealed the ultrafast excited-state dynamics of the Cu_{13} nanoclusters with three relaxation pathways.

Experimental section

Chemicals and materials

All the following reagents were purchased and used as received without further purification. Cuprous bromide (CuBr, 99%), sodium borohydride ($NaBH_4$, 98%), methanol (CH_3OH, analytical grade), toluene (C_7H_8, analytical grade) and n-hexane (C_6H_{14}, chromatographic grade) were purchased from Sinopharm Chemical Reagent Co. Ltd. Acetonitrile (CH_3CN, analytical grade) and dichloromethane (CH_2Cl_2, analytical grade) were purchased from Kermel. 2-Chloro-4-fluorobenzenethiol (C_6H_4ClFS, 97%) and triphenylphosphine (PPh_3, 99%) were purchased from Alfa Aesar. All glassware was cleaned with aqua regia (v(HCl)/v(HNO_3) = 3 : 1), rinsed with ultrapure water, and then dried in an oven prior to use.

Synthesis of $Cu_{13}H_{10}(SR)_3(PPh_3)_7$ nanoclusters

The Cu_{13} nanoclusters were prepared via a one-pot synthesis. 20 mg CuBr was dissolved in 10 mL CH_3CN in a round-bottom flask. The solution was stirred vigorously using a magnetic stirrer at room temperature. After about five minutes, 5 mL CH_3OH and 5 mL CH_2Cl_2 were added to the above solution. Subsequently, 37 mg PPh_3 was added. Then, 17 μL of 2-chloro-4-fluorobenzenethiol was added. After about 20 minutes, 100 mg $NaBH_4$ was added directly to the solution. About 10 minutes later, an orange-red precipitate was observed in the solution. After about 1 h, the precipitate was the crude product, and impurities in the supernatant were removed after centrifugation. Finally, the precipitate was dissolved in CH_2Cl_2 to extract the pure product. Of note, the product can also be prepared using CuCl or $CuCl_2 \cdot 2H_2O$ to replace CuBr, but the yield is lower than using CuBr.

Synthesis of $Cu_{13}D_{10}(SR)_3(PPh_3)_7$ nanoclusters

The deuterated Cu_{13} nanoclusters were prepared using the same procedure as the $Cu_{13}H_{10}(SR)_3(PPh_3)_7$ nanoclusters via replacing $NaBH_4$ with $NaBD_4$.

Single-crystal X-ray crystallography

Red block crystals of the Cu_{13} nanoclusters were grown in a mixture of CH_2Cl_2 and hexane in a 4 °C refrigerator. The X-ray crystallographic data of the Cu_{13} nanoclusters was collected using a single crystal X-ray diffractometer (Bruker D8 VENTURE) using Cu Kα radiation ($\lambda = 1.54178$ Å) at Shanghai Jiao Tong University. The structure was solved by direct methods and refined with full-matrix least squares on F2 using the SHELXTL software package and Olex2. All non-hydrogen atoms were refined anisotropically.[59–61] CCDC deposition number: 2170868.

Other physical measurements

The UV-vis spectra of Cu_{13} nanoclusters dissolved in CH_2Cl_2 were collected using a SHIMADZU UV-1800 spectrophotometer. The fluorescence spectra of the Cu_{13} nanoclusters were obtained using an Agilent Technologies Cary Eclipse Fluorescence

Spectrophotometer. The electrospray ionization mass spectrum (ESI-MS) of the nanoclusters dissolved in a mixture of toluene and methanol (v/v = 1/1) was collected using a Fourier Transform Ion Cyclotron Resonance Mass Spectrometer (SolariX XR-15T). Digital photos of the solution and crystals of the Cu_{13} nanoclusters were shot using an MI 8 AI dual camera. XPS was conducted using a Thermo Fisher ESCALAB 250xi. ^{1}H NMR and ^{2}H NMR spectroscopy were carried out using a Bruker AVANCE 400 MHz and AVANCE III HD 700 MHz, respectively.

Computational method

Density function theory calculations (DFT) were performed with the Gaussian 16 program package.[62] The structural optimizations were carried out with the wb97xd functional[63] and def2-SVP basis set.[64] NMR shielding tensors were computed using the Gauge-Independent Atomic Orbital (GIAO) method on the optimized geometries, and the chemical shifts were calculated using tetramethylsilane as the reference.[65] The electronic excitations were calculated using the time-dependent DFT method on the optimized geometries, and the UV-vis spectrum was simulated using a Gaussian broadening function with a full width at half maximum of 0.66667 eV.[66]

Results and discussion

Synthesis and crystallization

The $Cu_{13}H_{10}(SR)_3(PPh_3)_7$ nanoclusters were obtained *via* a solvent-mediated precipitating synthesis. First, CuBr was dissolved in CH_3CN, followed by the addition of CH_3OH and CH_2Cl_2 in the proper order. Next, PPh_3 and 2-chloro-4-fluorobenzenethiol were added successively. Finally, $NaBH_4$ was added directly to the above solution to reduce the Cu–ligand complexes. About 10 minutes later, an orange-red precipitate appeared in the solution (Fig. S1a†). After centrifugation, the supernate containing the excess or unreacted reagents was removed, and the precipitate was the target product. The yield of the product was high (39.5% based on Cu atom). It is worth mentioning that the prepared product was of high purity without further washing, proving the superiority of the SMPS strategy. Choosing different types of solvent is beneficial to the interfacial reaction and precipitation of the Cu nanoclusters. This method might represent a strategy to synthesize less-stable metal nanoclusters *via* modulating the reaction solvents, in which the metal nanoclusters have different solubilities. Red block crystals of the Cu_{13} nanoclusters (Fig. S1b–d†) were grown in a mixture of CH_2Cl_2 and hexane in a 4 °C refrigerator for 1–2 days (for details, see Experimental section). Using $NaBD_4$ to replace $NaBH_4$, the deuterated analogue ($Cu_{13}D_{10}(SR)_3(PPh_3)_7$, Cu_{13D} for short) was synthesized following the same procedure.

Crystal structure

The crystal structure of the Cu_{13} nanoclusters was determined using single crystal X-ray crystallography. The Cu_{13} nanoclusters crystallized in the trigonal crystal system with the $R\bar{3}$ space group, and twelve Cu_{13} nanoclusters are packed in a unit

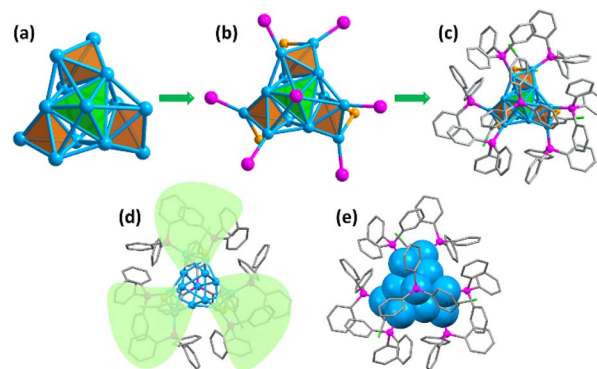Fig. 1 (a) The Cu_{13} kernel composed of four vertex-sharing tetrahedrons. (b) The Cu_{13} kernel with P and S atoms. (c−e) The total crystal structure of the $Cu_{13}H_{10}(SR)_3(PPh_3)_7$ nanoclusters presented in different styles. The three tetrahedrons at the bottom are marked in orange and the tetrahedron at the top is marked in green. Color code: blue, Cu; magenta, P; orange, S; green, Cl; grey, C. The hydrogen atoms are omitted for clarity.

cell (Table S1 and Fig. S2†). Fig. 1 shows the total crystal structure of the Cu_{13} nanoclusters with a threefold symmetry (C_3) axis. Four tetrahedrons constitute the aesthetic Cu_{13} kernel *via* sharing three vertices, which is different from the common M_{13} icosahedron or cuboctahedron structures (Fig. 1a). The tetrahedron at the top marked in green occupies the C_3 axis, and the three tetrahedrons in the bottom marked in orange are distributed symmetrically along the C_3 axis. The Cu_{13} metal kernel is encapsulated by 7 PPh_3 and 3 thiolates, and the total structure looks like a tri-blade fan (Fig. 1b–e), which is similar to that of Cu_{15} nanoclusters.[4]

Further structural investigation revealed that the Cu_{13} kernel could be divided into two layers (Fig. 2a and b). The first layer containing 7 Cu atoms looks like a hat from the front view, and is made up of four quadrilaterals from the top view (Fig. 2c and d). The second layer containing 6 Cu atoms is a propeller-like structural unit, which is a Cu_3 triangle connected to three single Cu atoms from the top view (Fig. 2e and f). The average Cu–Cu length of the Cu_{13} nanoclusters is 2.57 Å with a range

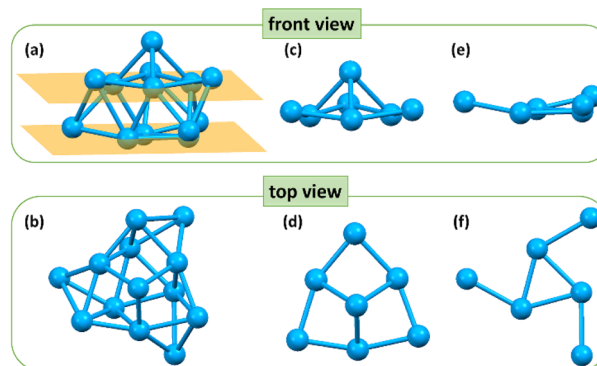Fig. 2 The front view and top view of (a and b) the skeleton structure, (c and d) first layer and (e and f) second layer of the $Cu_{13}H_{10}(SR)_3(PPh_3)_7$ nanoclusters. Color code: blue, Cu.

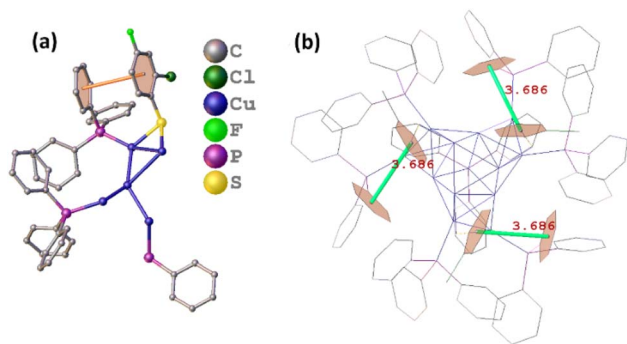**Fig. 3** The π···π interactions between thiolates and PPh₃ on the surface of the Cu₁₃H₁₀(SR)₃(PPh₃)₇ nanoclusters shown in the asymmetric unit (a) and total structure (b).

and 2.262–2.285 Å (average: 2.274 Å), respectively. The three Cu–S–Cu angles are 69.8° (Table S3†). It is worth mentioning that the weak inter-ligand interactions in the metal nanoclusters are important for the atomic construction of the surface structure and the unit cell packing arrangement. In the Cu₁₃ nanoclusters, the intramolecular π···π interactions with a short distance (3.686 Å) exist between the benzene rings of the thiolates and PPh₃ on the surface, resulting in the stable configuration (Fig. 3).

Molecular formula and chemical state

To further identify the molecular formula, electrospray ionization mass spectroscopy (ESI-MS) of the Cu₁₃ nanoclusters in positive mode was carried out using a Fourier transform ion cyclotron resonance mass spectrometer. As shown in Fig. 4a, a dominant peak with one positive charge was observed at $m/z = 3482.7$ in the mass spectrum. The inset spectra showed that the experimental value was highly consistent with the simulated isotopic distribution, corresponding to the formula [Cu₁₃H₁₀(SR)₃(PPh₃)₇ + Cu⁺ + PPh₃]⁺. To confirm the number of hydrogen atoms, the deuterated analogue was prepared using NaBD₄ as the reducing agent. The ESI-MS of the deuterated analogue shows a prominent peak at $m/z = 3492.7$, which was attributed to the formula [Cu₁₃D₁₀(SR)₃(PPh₃)₇ + Cu⁺ + PPh₃]⁺, thus indicating the existence of 10 hydride ligands in the Cu₁₃ nanoclusters (Fig. 4b).

X-ray photoelectron spectroscopy (XPS) was carried out to investigate the elemental composition and chemical states of

from 2.415 Å to 2.792 Å (Tables S2 and S3†), which is close to the Cu–Cu length of bulk Cu and lower than that of other reported Cu nanoclusters (Table S4†), indicating stronger Cu–Cu interactions.

With regard to the exterior protective monolayer of Cu₁₃ nanoclusters, each of the seven PPh₃ is directly connected to one Cu atom via a single Cu–P bond. One PPh₃ is located on the C₃ symmetry axis, and the other six PPh₃, along with the three thiolates, are arranged symmetrically around the C₃ axis (Fig. S3†). Each thiolate bonds with two Cu atoms in a low-coordinated μ₂-η¹, η¹ bridging mode (Fig. S4†). The Cu–P and Cu–S bond length ranges are 2.229–2.240 Å (average: 2.237 Å)

Fig. 4 The ESI-MS of Cu₁₃H₁₀(SR)₃(PPh₃)₇ (a) and Cu₁₃D₁₀(SR)₃(PPh₃)₇ (b) nanoclusters in positive mode. Insets show the experimental and simulated isotopic patterns. (c) The X-ray photoelectron full spectra of Cu₁₃H₁₀(SR)₃(PPh₃)₇ nanoclusters. Inset shows the XPS of Cu 2p. (d) ¹H NMR of Cu₁₃H₁₀(SR)₃(PPh₃)₇ (black) and ²H NMR of Cu₁₃D₁₀(SR)₃(PPh₃)₇ nanoclusters (red).

Cu_{13} nanoclusters. XPS spectra confirmed the presence of the expected elements Cu, S, P, F, Cl, and C (Fig. 4c). The inset exhibits the binding energy for Cu $2p_{1/2}$ at 952.7 eV and Cu $2p_{3/2}$ at 932.9 eV in the Cu_{13} nanoclusters. However, it is difficult to identify the chemical state of Cu owing to the same Cu $2p_{3/2}$ binding energy (932.6 eV) being observed for both Cu^0 and Cu^+ (Cu_2S) species.[4] The three Cu LMM peaks can be observed in the XPS, and the smallest binding energy is 570.0 eV, which is same as that of Cu_2O. The Cu LMM binding energy of Cu^0 is 568.0 eV.[67] Additionally, no satellite signal for Cu $2p_{3/2}$ from Cu(II) was observed at approximately 943 eV in the XPS spectra of Cu_{13} nanoclusters. Therefore, the chemical state of Cu in the Cu_{13} nanoclusters is close to that of Cu(I), which is consistent with that of other Cu nanoclusters.[4,54]

Nuclear magnetic resonance (NMR) was performed to identify the chemical shifts of the hydrides in the Cu_{13} nanoclusters. In the ^1H NMR spectra, Cu_{13} and Cu_{13D} nanoclusters exhibit similar peaks (Fig. S5†). The peaks at 8–6.4 ppm correspond to protons in the thiolates and PPh_3 phenyl groups. The broadening of peaks between 8 and 6.4 ppm is ascribed to the differences in the environments of the ligands (Fig. S5†). Moreover, the Cu_{13} nanoclusters show three additional peaks centered at 2.76, 2.60 and 0.57 ppm in the ^1H NMR spectrum, compared with the Cu_{13D} nanoclusters (Fig. S5† and 4d). The ratio of the areas of the three peaks at 2.76, 2.60 and 0.57 ppm is 6 : 3 : 1. Notably, the peak at 2.76 ppm is wide, probably because of the overlap of two peaks. To further determine the type and ratio of the hydrides, the ^2H NMR of Cu_{13} and Cu_{13D} were measured. In the ^2H NMR spectra, both the Cu_{13} and Cu_{13D} nanoclusters exhibit peaks at 7.26 and 1.57 ppm, corresponding to $CDCl_3$ and D_2O, respectively (Fig. S6†). However, the Cu_{13D} nanoclusters show four more peaks than the Cu_{13} nanoclusters; these peaks are centered at 2.86, 2.83, 2.68 and 0.66 ppm and correspond to the hydrides (Fig. S6† and 4d). The ratio of the areas of the four peaks at 2.86, 2.83, 2.68 and 0.66 ppm is 3 : 3 : 3 : 1. The two peaks at 2.86 and 2.83 ppm in the ^2H NMR spectrum are so close that they obviously overlap. Accordingly, it can be inferred that the wide peak at 2.76 ppm in the ^1H NMR spectrum is also due to the overlap of two peaks, considering the area and position of the peak (Table S5†). Therefore, combined with the ESI-MS results, the NMR data further demonstrates that it is reasonable that the Cu_{13} nanoclusters contain 10 hydrides, including four types of hydrides.

Modeling the hydride positions

To determine the hydride positions in the Cu_{13} nanoclusters, DFT calculations were carried out to optimize the geometric structure of the Cu_{13} nanoclusters. Instead of the widely used simplified model in which the H–SR ligands in the thiolates are replaced by $HS-CH_3$ to save computational resources, the full model with the entire Cu_{13} structure was used in this work to reproduce the effects of the ligands. This is especially important for our $Cu_{13}H_{10}(SR)_3(PPh_3)_7$ nanoclusters, since intramolecular $\pi\cdots\pi$ interactions exist between the benzene rings of the thiolate and PPh_3 ligands on the surface. The optimizations were based on the X-ray crystal structure (Fig. S7†), and the adopted
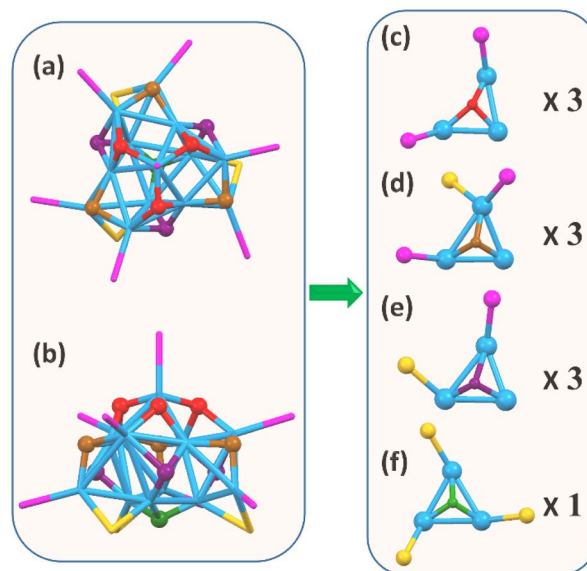

Fig. 5 The top view (a) and side view (b) of the optimized structure for the $Cu_{13}H_{10}(SR)_3(PPh_3)_7$ nanoclusters with the hydride sites in the kernel obtained from DFT calculations. (c–f) The hydrides binding with three Cu atoms can be seen to give four groups according to the triangular Cu_3 coordination environment. Color code: blue, Cu; magenta, P; orange, S; red/brown/purple/green, μ_3-H in the kernel. The carbon terminals of the ligands are omitted for clarity.

strategy is similar to that in a previous report.[54] First, only the hydrides were relaxed, and then both the hydrides and Cu were fully relaxed. Initial structures with μ_1, μ_2 and μ_3 hydrides were tried, and all of them optimized to the same structure (Table S7†). The optimized structure of the Cu_{13} nanoclusters is in accordance with the crystallographic structure (Fig. S8†). The simulated hydride sites in the optimized structure of the Cu_{13} nanoclusters are shown in Fig. 5a and b. Each of the 10 hydrides was connected to three Cu atoms in a μ_3 mode, and the hydrides could be categorized into four groups according to the triangular Cu_3 coordination environment. The number of hydrides located at the top, middle and bottom is 3, (3 + 3) and 1, respectively. First, the three hydrides marked in red at the top are bound to a Cu_3 triangle coordinated with two PPh_3 (Fig. 5c). Second, the three hydrides marked in brown at the middle are connected to Cu_3 triangles with one thiolate and two PPh_3 (Fig. 5d). Third, the three hydrides marked in purple at the middle are connected to a Cu_3 triangle with one thiolate and one PPh_3 (Fig. 5e). Fourth, the only hydride marked in green at the bottom is linked to a Cu_3 triangle with three thiolates (Fig. 5f). Of note, the two types of hydrides located at the middle have similar coordination environments, so they show nearly the same chemical shifts and their peaks overlap in the NMR spectra. The types and number of hydrides from the optimized structure are in good agreement with the NMR results.

Optical properties

The steady-state UV-vis absorption spectrum of the Cu_{13} nanoclusters exhibits four weak broad peaks at 305, 325, 340 and
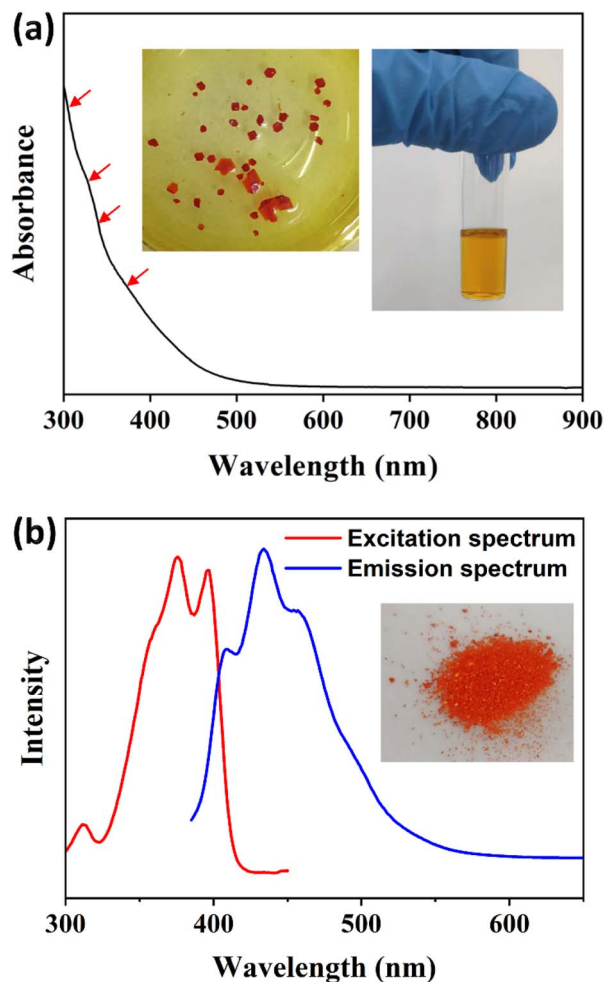
Fig. 6 (a) The UV-vis absorption spectrum of $Cu_{13}H_{10}(SR)_3(PPh_3)_7$ nanoclusters. The insets show the crystals and solution of the nanoclusters. (b) The excitation ($\lambda_{em} = 460$ nm) and emission ($\lambda_{ex} = 375$ nm) spectra of $Cu_{13}H_{10}(SR)_3(PPh_3)_7$ nanoclusters. The inset shows solid nanoclusters obtained via large-scale SMPS.

360 nm (Fig. 6a). The absorption peaks are not entirely obvious, which is a common phenomenon in Cu nanoclusters.[4,33,54,68] The UV-vis absorption spectrum was calculated using the time-dependent DFT method based on the entire structure of the Cu_{13} nanoclusters, and a decay curve can be observed (Fig. S9†). Actually, several absorption peaks at 300.9, 304.4, 311.8, 326.3, 328.2, 340.5, 342.4, 356.0 and 364.1 nm were predicted according to the oscillator strength (Fig. S9†). In summary, the calculated absorption peaks mainly lie in four approximate bands: 300–304 nm, 326–328 nm, 340–342 nm and 356–364 nm, which is in good agreement with the experimental spectrum. The Kohn–Sham molecular orbitals of the Cu_{13} nanoclusters are shown in Fig. S10.† The highest occupied molecular orbital (HOMO) and the lowest unoccupied molecular orbital (LUMO) are mainly composed of Cu and S atoms. Based on the maximum contribution to the absorption, the absorption peaks at 311.8, 328.2, 356.0 and 364.1 nm are attributed to the transition from Cu (3d) to Cu (4p). The other peaks arise from the transition between Cu (3d) and ligand π* (Table S6†).

The photoluminescence properties of the Cu_{13} nanoclusters were studied via fluorescence spectroscopy. As shown in Fig. 6b, the excitation spectrum shows three apparent peaks at 312, 375 and 396 nm with a shoulder at approximately 360 nm. Under excitation at 375 nm, the unique emission spectrum exhibits three obvious peaks at 408, 434 and 458 nm, respectively. Furthermore, we carried out fluorescence spectroscopy for the Cu_{13} nanoclusters at low temperatures (Fig. S11†). As the temperature decreases, the intensity of the photoluminescence increases. The blue emission of the Cu_{13} nanoclusters is remarkable, and will probably have promising applications such as cell labelling.[69–71] The photoluminescence might originate from the LMCT (ligand-to-metal charge transfer) process. The fluorescence is attributed to the electronic transition from the LUMO to the HOMO, and is mainly caused by charge transfer between the surface ligands with electron-donating capability and the Cu atoms with electron-withdrawing capability in the kernel.[72,73]

Exploring the excited-state dynamics of metal nanoclusters is essential to promote their practical applications. Femtosecond transient absorption spectroscopy was employed to study the excited-state properties of the Cu_{13} nanoclusters. The data map of the transient absorption spectrum as a function of the time delay after a 360 nm pump pulse is shown in Fig. 7a. It displays broad excited-state absorption (ESA) peaks at approximately 580 and 680 nm. Fig. 7b shows the transient absorption at different decay times, and the transient absorption signal decays almost to zero within 869.46 ps. Global fitting with a three-exponential-decay equation was applied to fit the time profile to analyze the ultrafast relaxation dynamics (Fig. 7c). To acquire good fitting quality, fitting the population dynamics of the transient absorption required three decay components: 1.1, 9.7, and 209 ps, respectively. This is similar to other metal
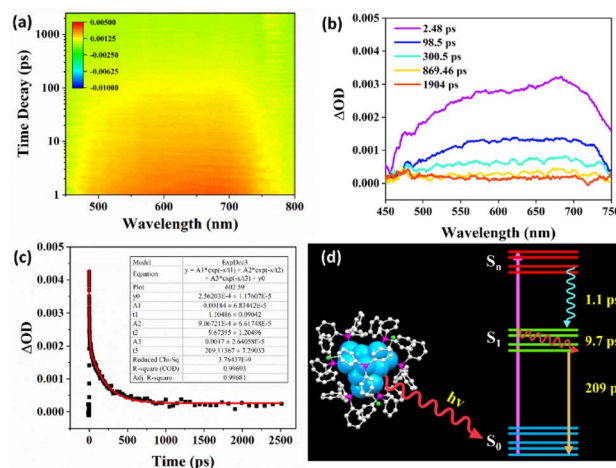
Fig. 7 (a) Transient absorption spectra data map of $Cu_{13}H_{10}(SR)_3(PPh_3)_7$ pumped at 360 nm. (b) Transient absorption spectra of $Cu_{13}H_{10}(SR)_3(PPh_3)_7$ at various times after excitation. (c) Kinetic traces monitored at around 600 nm (black) and curve fitting through the exponential equation (red). (d) The schematic illustration of the proposed relaxation dynamics of the $Cu_{13}H_{10}(SR)_3(PPh_3)_7$ nanoclusters.

nanoclusters.[68,74] Fig. 7d exhibits a schematic illustration of the proposed relaxation dynamics of the Cu_{13} nanoclusters. The ultrafast 1.1 ps component should be ascribed to the internal conversion from the S_n to the S_1 state. The 9.7 ps component can be attributed to the structural relaxation of vibrational cooling from hot S_1 to S_1, while the 209 ps component corresponds to the radiative relaxation from S_1 to the ground state S_0 (Fig. 7d). Revealing the excited-state relaxation dynamics of Cu_{13} nanoclusters is favorable for its applications in energy conversion and photoelectric applications.

Conclusions

In summary, a novel synthetic strategy named solvent-mediated precipitating synthesis (SMPS) was developed to prepare high-purity $Cu_{13}H_{10}(SR)_3(PPh_3)_7$ nanoclusters with high yield. The Cu_{13} nanoclusters comprise a Cu_{13} kernel and a monolayer of ligands including hydride, thiolate and PPh_3. The aesthetic Cu_{13} kernel consists of four rare vertex-sharing tetrahedrons, and the ligands are arranged symmetrically around the C_3 symmetry axis. The intramolecular $\pi\cdots\pi$ interactions between thiolates and PPh_3 on the surface are conducive to the stable configuration. The number, type and location of the 10 hydrides were revealed comprehensively. Furthermore, the Cu_{13} nanoclusters exhibit unique optical absorbance and photoluminescence. The transient absorption spectra revealed the ultrafast relaxation dynamics behaviors of internal conversion, structural relaxation and radiative relaxation of the Cu_{13} nanoclusters. This work provides an efficient strategy to synthesize a novel Cu nanocluster.

Data availability

We have provided the experimental and computational data in the ESI.†

Author contributions

X. L. conceived the project, designed the synthesis, and analyzed data. J. T., C. Z. and Y. Y. performed the measurements. L. W. and R. W. tested the ESI-MS. F. H. finished the DFT calculations. C. L. and J. H. conceived the project and provided the guidance. The manuscript was written through contributions of all authors. All authors have given approval to the final version of the manuscript.

Conflicts of interest

There are no conflicts to declare.

Acknowledgements

Notes and references

1 C. Dong, R. W. Huang, C. Chen, J. Chen, S. Nematulloev, X. Guo, A. Ghosh, B. Alamer, M. N. Hedhili, T. T. Isimjan, Y. Han, O. F. Mohammed and O. M. Bakr, *J. Am. Chem. Soc.*, 2021, **143**, 11026–11035.

2 S. Lee, M. S. Bootharaju, G. Deng, S. Malola, H. Hakkinen, N. Zheng and T. Hyeon, *J. Am. Chem. Soc.*, 2021, **143**, 12100–12107.

3 L. L. M. Zhang, G. D. Zhou, G. Q. Zhou, H. K. Lee, N. Zhao, O. V. Prezhdo and T. C. W. Mak, *Chem. Sci.*, 2019, **10**, 10122–10128.

4 S. Nematulloev, R. W. Huang, J. Yin, A. Shkurenko, C. Dong, A. Ghosh, B. Alamer, R. Naphade, M. N. Hedhili, P. Maity, M. Eddaoudi, O. F. Mohammed and O. M. Bakr, *Small*, 2021, **17**, e2006839.

5 B.-L. Han, Z. Liu, L. Feng, Z. Wang, R. K. Gupta, C. M. Aikens, C. H. Tung and D. Sun, *J. Am. Chem. Soc.*, 2020, **142**, 5834–5841.

6 J. C. Li, Y. Kuang, Y. T. Meng, X. Tian, W. H. Hung, X. Zhang, A. W. Li, M. Q. Xu, W. Zhou, C. S. Ku, C. Y. Chiang, G. Z. Zhu, J. Y. Guo, X. M. Sun and H. J. Dai, *J. Am. Chem. Soc.*, 2020, **142**, 7276–7282.

7 Y. H. Wang, A. Xu, Z. Y. Wang, L. S. Huang, J. Li, F. W. Li, J. Wicks, M. C. Luo, D. H. Nam, C. S. Tan, Y. Ding, J. W. Wu, Y. W. Lum, C. T. Dinh, D. Sinton, G. F. Zheng and E. H. Sargent, *J. Am. Chem. Soc.*, 2020, **142**, 5702–5708.

8 C. A. Chen, S. C. Chen, M. J. A. Shiddiky, C. F. Chen and K. C. W. Wu, *Chem. Rec.*, 2020, **20**, 174–186.

9 F. Peng, Y. Sun, Y. Lu, W. W. Yu, M. Y. Ge, J. C. Shi, R. Cong, J. M. Hao and N. Dai, *Nanomaterials*, 2020, **10**, 774.

10 P. P. Yang, X. L. Zhang, F. Y. Gao, Y. R. Zheng, Z. Z. Niu, X. X. Yu, R. Liu, Z. Z. Wu, S. Qin, L. P. Chi, Y. Duan, T. Ma, X. S. Zheng, J. F. Zhu, H. J. Wang, M. R. Gao and S. H. Yu, *J. Am. Chem. Soc.*, 2020, **142**, 6400–6408.

11 L. Zhang, X. X. Li, Z. L. Lang, Y. Liu, J. Liu, L. Yuan, W. Y. Lu, Y. S. Xia, L. Z. Dong, D. Q. Yuan and Y. Q. Lan, *J. Am. Chem. Soc.*, 2021, **143**, 3808–3816.

12 Q. Yao, Z. Wu, Z. Liu, Y. Lin, X. Yuan and J. Xie, *Chem. Sci.*, 2021, **12**, 99–127.

13 C. Sun, B. K. Teo, C. Deng, J. Lin, G. G. Luo, C. H. Tung and D. Sun, *Coord. Chem. Rev.*, 2021, **427**, 213576.

14 W. J. Zhang, Z. Liu, K. P. Song, C. M. Aikens, S. S. Zhang, Z. Wang, C. H. Tung and D. Sun, *Angew. Chem., Int. Ed.*, 2021, **60**, 4231–4237.

15 Y. Li and R. Jin, *J. Am. Chem. Soc.*, 2020, **142**, 13627–13644.

16 Y. Zhou, L. Liao, S. Zhuang, Y. Zhao, Z. Gan, W. Gu, J. Li, H. Deng, N. Xia and Z. Wu, *Angew. Chem., Int. Ed.*, 2021, **60**, 8668–8672.

17 M. W. Heaven, A. Dass, P. S. White, K. M. Holt and R. W. Murray, *J. Am. Chem. Soc.*, 2008, **130**, 3754–3755.

18 M. Zhu, C. M. Aikens, F. J. Hollander, G. C. Schatz and R. Jin, *J. Am. Chem. Soc.*, 2008, **130**, 5883–5885.

19 Y. Cao, V. Fung, Q. Yao, T. Chen, S. Zang, D. E. Jiang and J. Xie, *Nat. Commun.*, 2020, **11**, 5498.

20 Y. Zhao, S. Zhuang, L. Liao, C. Wang, N. Xia, Z. Gan, W. Gu, J. Li, H. Deng and Z. Wu, *J. Am. Chem. Soc.*, 2020, **142**, 973–977.

21 H. F. Qian, Y. Zhu and R. C. Jin, *J. Am. Chem. Soc.*, 2010, **132**, 4583–4585.

22 C. Zeng, Y. Chen, C. Liu, K. Nobusada, N. L. Rosi and R. Jin, *Sci. Adv.*, 2015, **1**, e1500425.

23 Z. Gan, Y. Liu, L. Wang, S. Jiang, N. Xia, Z. Yan, X. Wu, J. Zhang, W. Gu, L. He, J. Dong, X. Ma, J. Kim, Z. Wu, Y. Xu, Y. Li and Z. Wu, *Nat. Commun.*, 2020, **11**, 5572.

24 Z. B. Gan, J. S. Chen, L. W. Liao, H. W. Zhang and Z. K. Wu, *J. Phys. Chem. Lett.*, 2018, **9**, 204–208.

25 L. Liao, J. Chen, C. Wang, S. Zhuang, N. Yan, C. Yao, N. Xia, L. Li, X. Bao and Z. Wu, *Chem. Commun.*, 2016, **52**, 12036–12039.

26 C. J. Zeng, C. Liu, Y. X. Chen, N. L. Rosi and R. C. Jin, *J. Am. Chem. Soc.*, 2016, **138**, 8710–8713.

27 J. Q. Wang, S. Shi, R. L. He, S. F. Yuan, G. Y. Yang, G. J. Liang and Q. M. Wang, *J. Am. Chem. Soc.*, 2020, **142**, 18086–18092.

28 N. A. Sakthivel, S. Theivendran, V. Ganeshraj, A. G. Oliver and A. Dass, *J. Am. Chem. Soc.*, 2017, **139**, 15450–15459.

29 C. P. Joshi, M. S. Bootharaju, M. J. Alhilaly and O. M. Bakr, *J. Am. Chem. Soc.*, 2015, **137**, 11578–11581.

30 H. Yang, J. Yan, Y. Wang, G. Deng, H. Su, X. Zhao, C. Xu, B. K. Teo and N. Zheng, *J. Am. Chem. Soc.*, 2017, **139**, 16113–16116.

31 L. Ren, P. Yuan, H. Su, S. Malola, S. Lin, Z. Tang, B. K. Teo, H. Hakkinen, L. Zheng and N. Zheng, *J. Am. Chem. Soc.*, 2017, **139**, 13288–13291.

32 H. Y. Yang, Y. Wang, X. Chen, X. J. Zhao, L. Gu, H. Q. Huang, J. Z. Yan, C. F. Xu, G. Li, J. C. Wu, A. J. Edwards, B. Dittrich, Z. C. Tang, D. D. Wang, L. Lehtovaara, H. Hakkinen and N. F. Zheng, *Nat. Commun.*, 2016, **7**, 12809.

33 H. Li, H. Zhai, C. Zhou, Y. Song, F. Ke, W. W. Xu and M. Zhu, *J. Phys. Chem. Lett.*, 2020, **11**, 4891–4896.

34 B. Santiago-Gonzalez, A. Monguzzi, C. Capitani, M. Prato, C. Santambrogio, F. Meinardi and S. Brovelli, *Angew. Chem., Int. Ed.*, 2018, **57**, 7051–7055.

35 K. K. Chakrahari, R. P. B. Silalahi, J. H. Liao, S. Kahlal, Y. C. Liu, J. F. Lee, M. H. Chiang, J. Y. Saillard and C. W. Liu, *Chem. Sci.*, 2018, **9**, 6785–6795.

36 F. Ke, Y. B. Song, H. Li, C. J. Zhou, Y. X. Du and M. Z. Zhu, *Dalton Trans.*, 2019, **48**, 13921–13924.

37 K. K. Chakrahari, J. H. Liao, S. Kahlal, Y. C. Liu, M. H. Chiang, J. Y. Saillard and C. W. Liu, *Angew. Chem., Int. Ed.*, 2016, **55**, 14704–14708.

38 P. L. Rodriguez-Kessler, M. Rojas-Poblete and A. Munoz-Castro, *Phys. Chem. Chem. Phys.*, 2021, **23**, 18035–18043.

39 Z. Chen, Y. Wang, L. Liu, Z. Zhang and F. Liang, *Chem. Commun.*, 2012, **48**, 11689–11691.

40 T. A. Nguyen, Z. R. Jones, B. R. Goldsmith, W. R. Buratto, G. Wu, S. L. Scott and T. W. Hayton, *J. Am. Chem. Soc.*, 2015, **137**, 13319–13324.

41 A. W. Cook, Z. R. Jones, G. Wu, S. L. Scott and T. W. Hayton, *J. Am. Chem. Soc.*, 2018, **140**, 394–400.

42 R. S. Dhayal, J. H. Liao, Y.-R. Lin, P.-K. Liao, S. Kahlal, J. Y. Saillard and C. W. Liu, *J. Am. Chem. Soc.*, 2013, **135**, 4704–4707.

43 R. S. Dhayal, J. H. Liao, X. Wang, Y. C. Liu, M. H. Chiang, S. Kahlal, J. Y. Saillard and C. W. Liu, *Angew. Chem., Int. Ed.*, 2015, **54**, 13604–13608.

44 R.-W. Huang, J. Yin, C. Dong, P. Maity, M. N. Hedhili, S. Nematulloev, B. Alamer, A. Ghosh, O. F. Mohammed and O. M. Bakr, *ACS Mater. Lett.*, 2020, **3**, 90–99.

45 S. Maity, D. Bain, S. Chakraborty, S. Kolay and A. Patra, *ACS Sustainable Chem. Eng.*, 2020, **8**, 18335–18344.

46 F. Li and Q. Tang, *J. Catal.*, 2020, **387**, 95–101.

47 A. Chen, X. Kang, S. Jin, W. Du, S. Wang and M. Zhu, *J. Phys. Chem. Lett.*, 2019, **10**, 6124–6128.

48 A. J. Edwards, R. S. Dhayal, P. K. Liao, J. H. Liao, M. H. Chiang, R. O. Piltz, S. Kahlal, J. Y. Saillard and C. W. Liu, *Angew. Chem., Int. Ed.*, 2014, **53**, 7214–7218.

49 R. S. Dhayal, J. H. Liao, S. Kahlal, X. Wang, Y. C. Liu, M. H. Chiang, W. E. van Zyl, J. Y. Saillard and C. W. Liu, *Chem.–Eur. J.*, 2015, **21**, 8369–8374.

50 S. Lee, M. S. Bootharaju, G. Deng, S. Malola, W. Baek, H. Hakkinen, N. Zheng and T. Hyeon, *J. Am. Chem. Soc.*, 2020, **142**, 13974–13981.

51 P. Yuan, R. H. Chen, X. M. Zhang, F. J. Chen, J. Z. Yan, C. F. Sun, D. H. Ou, J. Peng, S. C. Lin, Z. C. Tang, B. K. Teo, L. S. Zheng and N. F. Zheng, *Angew. Chem., Int. Ed.*, 2019, **58**, 835–839.

52 M. Qu, F. Q. Zhang, D. H. Wang, H. Li, J. J. Hou and X. M. Zhang, *Angew. Chem., Int. Ed.*, 2020, **59**, 6507–6512.

53 A. Ghosh, R.-W. Huang, B. Alamer, E. Abou-Hamad, M. N. Hedhili, O. F. Mohammed and O. M. Bakr, *ACS Mater. Lett.*, 2019, **1**, 297–302.

54 R. W. Huang, J. Yin, C. Dong, A. Ghosh, M. J. Alhilaly, X. Dong, M. N. Hedhili, E. Abou-Hamad, B. Alamer, S. Nematulloev, Y. Han, O. F. Mohammed and O. M. Bakr, *J. Am. Chem. Soc.*, 2020, **142**, 8696–8705.

55 M. Brust, M. Walker, D. Bethell, D. J. Schiffrin and R. Whyman, *J. Chem. Soc., Chem. Commun.*, 1994, 801–802.

56 W. Wei, Y. Lu, W. Chen and S. Chen, *J. Am. Chem. Soc.*, 2011, **133**, 2060–2063.

57 A. Baghdasaryan and T. Burgi, *Nanoscale*, 2021, **13**, 6283–6340.

58 X. Liu and D. Astruc, *Coord. Chem. Rev.*, 2018, **359**, 112–126.

59 G. M. Sheldrick, *Acta Crystallogr., Sect. A: Found. Crystallogr.*, 2008, **64**, 112–122.

60 O. V. Dolomanov, L. J. Bourhis, R. J. Gildea, J. A. K. Howard and H. Puschmann, *J. Appl. Crystallogr.*, 2009, **42**, 339–341.

61 G. M. Sheldrick, *Acta Crystallogr., Sect. C: Struct. Chem.*, 2015, **71**, 3–8.

62 M. J. Frisch, G. W. Trucks, H. B. Schlegel, G. E. Scuseria, M. A. Robb, J. R. Cheeseman, G. Scalmani, V. Barone, G. A. Petersson and H. Nakatsuji, *et al.*, *Gaussian 16 program package*, Gaussian, Inc., Wallingford CT, 2016.

63 J. D. Chai and M. Head-Gordon, *Phys. Chem. Chem. Phys.*, 2008, **10**, 6615–6620.

64 F. Weigend and R. Ahlrichs, *Phys. Chem. Chem. Phys.*, 2005, **7**, 3297–3305.

65 K. Wolinski, J. F. Hinton and P. Pulay, *J. Am. Chem. Soc.*, 1990, **112**, 8251–8260.

66 T. Lu and F. W. Chen, *J. Comput. Chem.*, 2012, **33**, 580–592.

67 I. Platzman, R. Brener, H. Haick and R. Tannenbaum, *J. Phys. Chem. C*, 2008, **112**, 1101–1108.

68 S. Maity, D. Bain, K. Bhattacharyya, S. Das, R. Bera, B. Jana, B. Paramanik, A. Datta and A. Patra, *J. Phys. Chem. C*, 2017, **122**, 13354–13362.

69 R. Ghosh, A. K. Sahoo, S. S. Ghosh, A. Paul and A. Chattopadhyay, *ACS Appl. Mater. Interfaces*, 2014, **6**, 3822–3828.

70 Z. G. Wang, B. K. Chen and A. L. Rogach, *Nanoscale Horiz.*, 2017, **2**, 135–146.

71 Y. e. Shi, J. Ma, A. Feng, Z. Wang and A. L. Rogach, *Aggregate*, 2021, **2**, e112.

72 X. Kang and M. Zhu, *Chem. Soc. Rev.*, 2019, **48**, 2422–2457.

73 X. Kang, S. X. Wang, Y. B. Song, S. Jin, G. D. Sun, H. Z. Yu and M. Z. Zhu, *Angew. Chem., Int. Ed.*, 2016, **55**, 3611–3614.

74 T. Higaki, C. Liu, M. Zhou, T. Y. Luo, N. L. Rosi and R. C. Jin, *J. Am. Chem. Soc.*, 2017, **139**, 9994–10001.